

Sub-micrometer phonon mean free paths in metal-organic frameworks revealed by machine-learning molecular dynamics simulations

Penghua Ying,^{1,*} Ting Liang,² Ke Xu,³ Jin Zhang,¹ Jianbin Xu,² Zheng Zhong,¹ and Zheyong Fan^{4,†}

¹*School of Science, Harbin Institute of Technology, Shenzhen, 518055, P. R. China*

²*Department of Electronic Engineering and Materials Science and Technology Research Center, The Chinese University of Hong Kong, Shatin, N.T., Hong Kong SAR, 999077, P. R. China*

³*Department of Physics, Xiamen University, Xiamen 361005, P. R. China.*

⁴*College of Physical Science and Technology, Bohai University, Jinzhou 121013, P. R. China*

(Dated: June 6, 2023)

Metal-organic frameworks (MOFs) are a family of materials that have high porosity and structural tunability and hold great potential in various applications, many of which requiring a proper understanding of the thermal transport properties. Molecular dynamics (MD) simulations play an important role in characterizing the thermal transport properties of various materials. However, due to the complexity of the structures, it is difficult to construct accurate empirical interatomic potentials for reliable MD simulations of MOFs. To this end, we develop a set of accurate yet highly efficient machine-learned potentials for three typical MOFs, including MOF-5, HKUST-1, and ZIF-8, using the neuroevolution potential approach as implemented in the GPUMD package, and perform extensive MD simulations to study thermal transport in the three MOFs. Although the lattice thermal conductivity (LTC) values of the three MOFs are all predicted to be smaller than 1 W/(m K) at room temperature, the phonon mean free paths (MFPs) are found to reach the sub-micrometer scale in the low-frequency region. As a consequence, the apparent LTC only converges to the diffusive limit for micrometer single crystals, which means that the LTC is heavily reduced in nanocrystalline MOFs. The sub-micrometer phonon MFPs are also found to be correlated with a moderate temperature dependence of LTC between those in typical crystalline and amorphous materials. Both the large phonon MFPs and the moderate temperature dependence of LTC fundamentally change our understanding of thermal transport in MOFs.

I. INTRODUCTION

In the last two decades, due to their ultra-high porosity [1] and structural tunability [2], metal-organic frameworks (MOFs) have shown great potential in various applications, such as gas storage and separation [3], water harvesting [4], electronic devices [5], and heterogeneous catalysis [6]. Lattice thermal conductivity (LTC) is a critical parameter for MOFs in the context of thermal energy conversion, thermal management and thermal stability and has attracted extensive experimental [7–15] and theoretical [16–37] studies.

It is generally difficult to produce large-scale single crystals of MOFs which then usually exist in the form of powders. The small crystalline sizes present a great challenge for experimentally measuring the LTC of MOF crystals [13] because the contact thermal resistance between the crystalline particles can introduce large systematic errors. Despite this, single-crystalline MOF-5 [38] can be grown up to a linear dimension of a couple of millimeter and its LTC has been measured to be 0.32 W/(m K) [7] using the steady-state direct method. Recent advances in experimental techniques also enabled the measurement of the LTC of a few typical MOFs in single-crystal form. For example, the LTC of single-crystal ZIF-8 [39] was measured to be

0.64 ± 0.09 W/(m K), using the Raman-resistance temperature detectors method [14]. For HKUST-1 [40], a value of 0.69 ± 0.05 W/(m K) was determined based on the thermoreflectance method [15].

Computationally, molecular dynamics (MD) simulation has played an important role in calculating the LTC and revealing the underlying mechanics for thermal transport in MOFs. Both the equilibrium molecular dynamics (EMD) [41, 42] and the non-equilibrium molecular dynamics (NEMD) methods have been extensively used. However, results from these two methods seem to be conflicting. For example, a weak temperature dependence of LTC in MOF-5 has been predicted using EMD simulations, which was attributed to short phonon mean free paths (MFPs) on the order of the lattice parameter [16]. Similarly, for ZIF-4 and ZIF-62, it has been suggested, based on EMD simulations [34, 35], that the phonon transport are strongly localized with phonon MFPs less than 1.5 nm. However, recent NEMD simulations suggested that the LTC of MOF-5 is actually not fully converged even when the transport length exceeds 20 nm [33, 36] and phonons with MFPs larger than 100 nm exist in HKUST-1 [37].

The differences in the results could be partially attributed to the different interatomic potentials used in different works, but there are two other possible causes. On the one hand, the heat current as implemented in the LAMMPS package [44] used in most of the previous EMD simulations [17, 18, 23–25, 28, 29, 34, 35] was incorrect for many-body potentials, which could lead to significantly

* hityingph@163.com

† brucenju@gmail.com

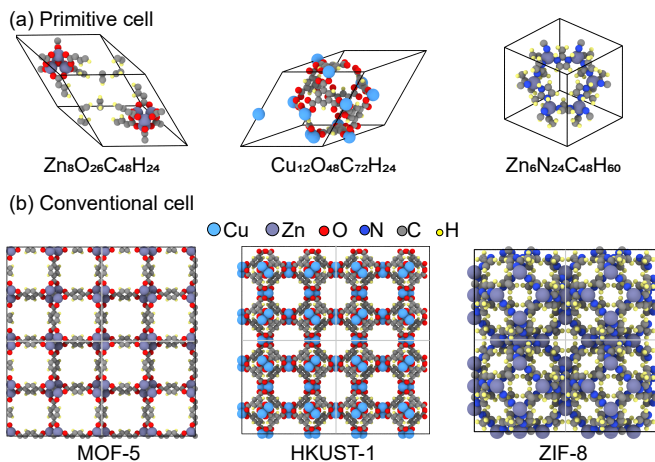


FIG. 1. The (a) primitive and (b) $2 \times 2 \times 2$ conventional cells of MOF-5 (left), HKUST-1 (middle), and ZIF-8 (right). The primitive cells contain 106, 156, and 138 atoms and the $2 \times 2 \times 2$ conventional ones contain 3992, 4992, and 2208 atoms. MOF-5 [38] is formed by connecting Zn_4O clusters with 1,4-benzenedicarboxylate organic linkers, resulting in a primitive cubic net topology. HKUST-1 [40] features copper paddle wheel units connected by 1,3,5-benzenetricarboxylate organic linkers, creating a body-centered cubic net topology. Lastly, ZIF-8 [39] comprises of tetrahedral ZnN_4 nodes connected by 2-methylimidazolate organic linkers, generating a sodalite net topology. We use primitive cells to prepare the reference datasets for training. For the calculation of LTC in MD simulations, we employ conventional cells of various system sizes. The OVITO package [43] was used for visualization.

reduced LTC and phonon MFPs in systems with low-dimensional features [45]. On the other hand, it is often assumed that a supercell with $2 \times 2 \times 2$ conventional cells is sufficient to obtain convergent results in EMD simulations [16–18, 23, 24, 28, 29], which is not necessarily valid. It is important to resolve the conflict between the EMD and the NEMD methods and obtain a clear and consistent picture of the phonon MFPs in MOFs because phonon MFPs determine the variation of the apparent LTC with respect to the sample length, which, in the context of MOFs, can be the grain size of polycrystals or the linear size of the clusters in MOF powders.

In this paper, we present a coherent understanding of the phonon MFPs in MOFs by considering three typical MOFs, including MOF-5 [38], HKUST-1 [40], and ZIF-8 [39], as shown in Fig. 1. To this end, we construct accurate interatomic potentials for these materials by training state-of-the-art machine-learned potentials (MLPs) against quantum-mechanical density functional theory (DFT) calculations. Recently, MLPs have been successfully applied to study a variety of properties of MOFs such as mechanical properties [46], phase transition [47], and gas diffusion [48, 49]. Herein, we choose to use the neuroevolution potential (NEP) approach [50–52] that has been demonstrated to be highly efficient while being also sufficiently accurate. Moreover,

the NEP approach has been implemented in the GPUMD package [53], which has the correct implementation of the heat current [45]. We perform large-scale MD simulations to study thermal transport, establishing a coherent picture of thermal transport in MOFs by using three MD methods, including the aforementioned EMD and NEMD and a third one, namely, the homogeneous non-equilibrium molecular dynamics (HNEMD) method [54]. Our results show that in all the three MOFs, the phonon MFPs can reach the sub-micrometer scale in the low-frequency region, which indicates that the LTC will be significantly reduced in polycrystals or powders with nanometer-scale grain sizes.

II. RESULTS AND DISCUSSION

A. Performance evaluation of the NEP models

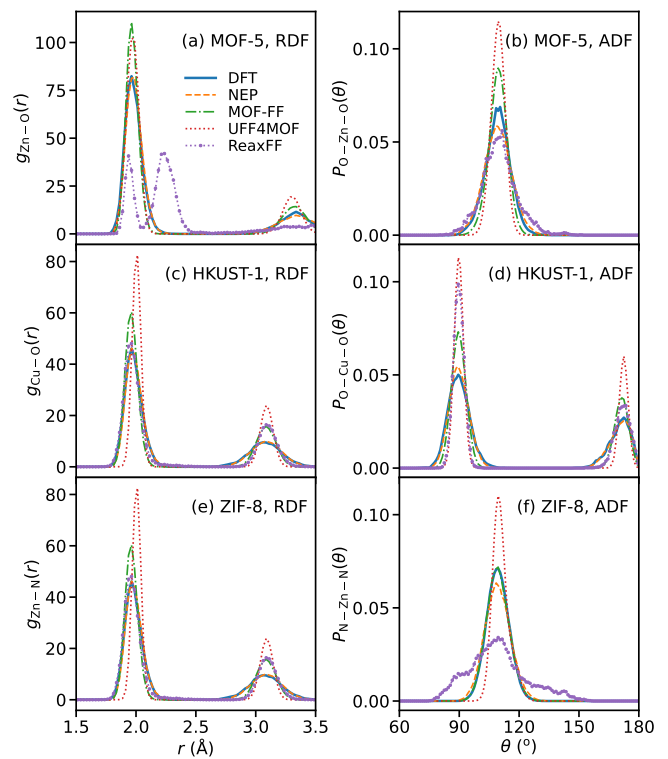


FIG. 2. Typical RDFs (left) and ADFs (right) in MOF-5 (top), HKUST-1 (middle), and ZIF-8 (bottom) calculated using classical MD simulations at 300 K driven by DFT, NEP, UFF4MOF [55, 56], MOF-FF [57–59], and ReaxFF [60–62].

We employed an iterative approach to develop machine-learned NEP models, as illustrated in Fig. S1 (see Sect. 2 for details). The NEP models for all the three MOFs achieve very high accuracy, with root mean square errors (RMSEs) of energy, force, and virial being less than 0.6 meV/atom, 60 meV/Å, and 5 meV/atom, respectively, for both the training and test data sets (see

Fig. S2 and Table S1 for details). The zero-temperature lattice constants predicted by the NEP models closely match those predicted by DFT calculations, with a relatively error being less than 0.1 % (see Table S2 for details).

To further evaluate the accuracy of the NEP models in MD simulations, we compare the RDFs and ADFs of the three MOFs at 300 K calculated from the NEP models with those obtained from DFT and a few representative empirical force fields (see Fig. 2). The selected force fields include MOF-FF [58], UFF4MOF [55], and ReaxFF [63], which have been widely used in MD simulation of the thermodynamics of MOF-5 [57, 64, 65], HKUST-1 [65–67], and ZIF-8 [24, 28, 65].

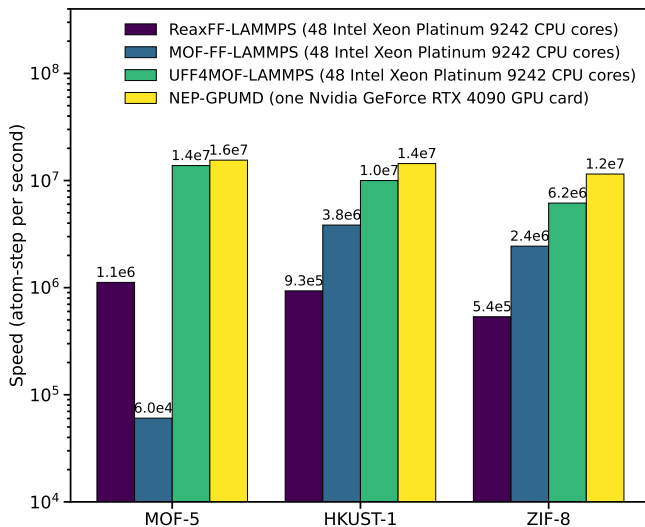


FIG. 3. Computational speeds of the NEP models as implemented in GPUMD [53] (version 3.7, running with an Nvidia GeForce RTX 4090 GPU card) and several empirical force fields as implemented in LAMMPS [44] (version 28 Mar 2023, running with 48 Intel Xeon Platinum 9242 CPU cores) for the three MOFs. The benchmark was performed using a $5 \times 5 \times 5$ supercell containing 53 000, 78 000, and 34 500 atoms for MOF-5, HKUST-1, and ZIF-8, respectively.

For RDF, we considered the most important pairs at the metal-linker interfaces: Zn-O in MOF-5, Cu-O in HKUST-1, and Zn-N in ZIF-8. Accordingly, we considered the O-Zn-O, O-Cu-O, and N-Zn-N triplets for the ADF. For both RDF and ADF, NEP achieves excellent agreement with DFT, while the empirical force fields exhibit varying degrees of discrepancies compared to DFT. Among the three selected empirical force fields, MOF-FF achieves the highest accuracy and the other two are much less accurate. UFF4MOF predicts inaccurate positions for some RDF peaks and too sharp peaks in the ADFs, while ReaxFF predicts a non-existing peak in the RDF of MOF-5 and too flat ADF of ZIF-8. The inaccuracies of ReaxFF in MD simulations of ZIFs have also been highlighted elsewhere [68].

Our NEP models not only achieve high accuracy, but

also have high computational efficiency. As can be seen from Fig. 3, the NEP models as implemented in GPUMD [53] running with a single Nvidia GeForce RTX 4090 GPU card are faster than all the empirical force fields as implemented in LAMMPS [44] running with 48 Intel Xeon Platinum 9242 CPU cores. The MOF-FF force field for MOF-5 [57] is particularly slow because it evaluates the Coulomb potential using the expensive Ewald summation. Apart from this, the computational speed of MOF-FF is higher than that of ReaxFF and lower than that of UFF4MOF.

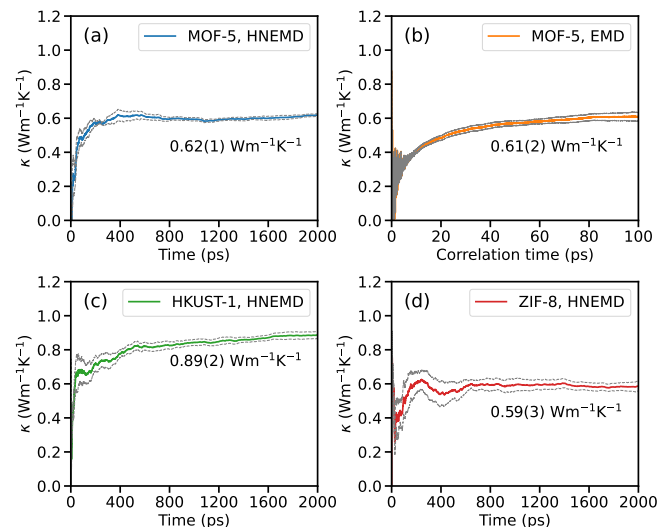


FIG. 4. Cumulative average of the LTC as calculated using the HNEMD method for (a) MOF-5, (c) HKUST-1, and (d) ZIF-8 at 300 K. (b) Running LTC as calculated using the EMD method for MOF-5. The simulation cells contain $5 \times 5 \times 5$ conventional cells. In each panel, the middle line represents the average and the other two represent the upper and lower bounds as calculated from five independent runs.

B. Thermal transport in MOFs

After confirming the reliability of our NEP models in MD simulations, we apply them to calculate the LTC using the various MD methods as reviewed in Sect. III. In Fig. 4 we show the HNEMD and EMD results for the three MOFs at 300 K and zero pressure obtained by using a supercell with $5 \times 5 \times 5$ conventional cells. In both methods, the LTC has converged with respect to the production or correlation time. The results from the two methods are consistent as expected based on their physical equivalence [54]. However, we note that even if the total production time we used for the EMD method for each system (50 ns) is much larger than that for the HNEMD method (10 ns), the latter still has smaller statistical errors, which demonstrates the superior computational efficiency of the HNEMD method [54].

In both the HNEMD and the EMD methods, peri-

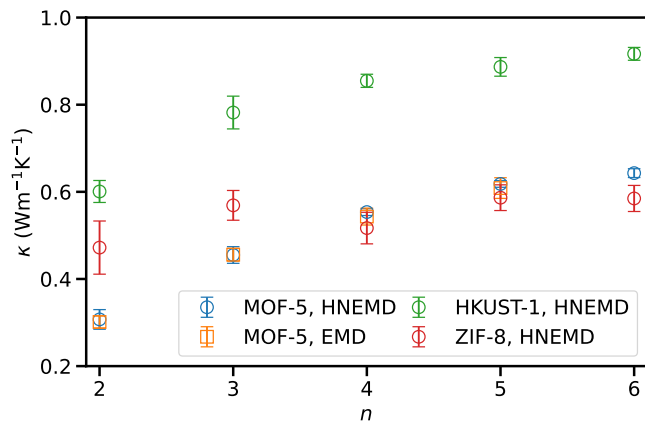


FIG. 5. LTC κ as a function of the number of conventional cells n in one direction of a cubic supercell for the three MOFs at 300 K from the HNEMD and EMD (for MOF-5 only) simulations.

odic boundary conditions are applied in the three directions and the results are regarded as those for infinitely large systems. However, this requires to eliminate the finite-size effects by using a sufficiently large supercell. While previous works often assumed that a supercell with $2 \times 2 \times 2$ conventional cells is sufficient to obtain convergent results in EMD simulations [16–18, 23, 24, 28, 29], our results in Fig. 5 show that for all the three MOFs, a supercell with $5 \times 5 \times 5$ conventional cells is required to converge the LTC. Note that agreement between the HNEMD and the EMD methods for MOF-5 are confirmed for all the simulation domains up to the $5 \times 5 \times 5$ supercell.

TABLE I. LTCs (in units of W/(m K)) of MOF-5 calculated by using the HNEMD method with different supercell sizes at different temperatures. The numbers within the parentheses are statistical uncertainties for the last significant number.

Supercells	200 K	250 K	300 K	350 K	400 K
$2 \times 2 \times 2$	0.38(4)	0.36(4)	0.31(2)	0.31(2)	0.31(2)
$5 \times 5 \times 5$	0.76(1)	0.72(2)	0.62(1)	0.55(1)	0.51(2)

Several studies have predicted a weak temperature dependence of the LTC of MOF-5 [16] and various ZIF materials, such as ZIF-8 [17, 28], ZIF-4 [35], and ZIF-62 [35], using a small supercell in EMD simulations. With the small $2 \times 2 \times 2$ supercell, we also obtained a weak temperature dependence of the LTC of MOF-5 as shown in Fig. 6 and Table I. Particularly, the LTC is almost a constant from 300 to 400 K. However, using the converged $5 \times 5 \times 5$ supercell, a notable temperature dependence of $\sim T^{-0.6}$ is obtained. This again highlights the importance of using a sufficiently large supercell in EMD and HNEMD simulations.

The calculated LTC values at 300 K using the converged $5 \times 5 \times 5$ supercell are listed in Table II. Our predicted LTC of ZIF-8, 0.59 ± 0.03 W/(m K), closely

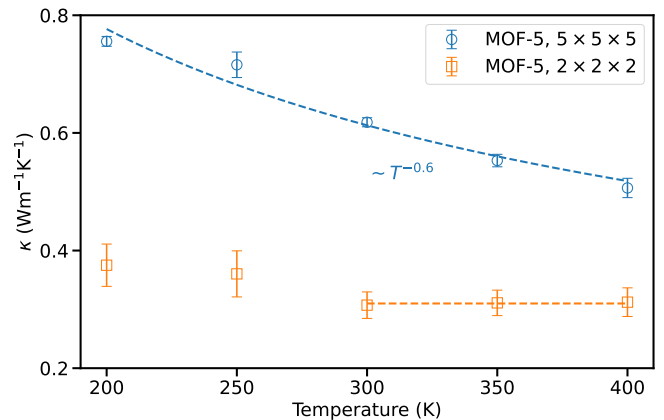


FIG. 6. LTC κ as a function of temperature for MOF-5 as obtained by using the $5 \times 5 \times 5$ and $2 \times 2 \times 2$ supercells. The dashed line for the case of $5 \times 5 \times 5$ supercell indicates a $\sim T^{-0.6}$ fitting, and the dashed line for the case of $2 \times 2 \times 2$ supercell indicates that the LTC is a constant from 300 to 400 K.

TABLE II. LTCs (in units of W/(m K)) of the three MOFs calculated by using the HNEMD method and EMD method (for MOF-5 only) with different supercell sizes (the number of conventional cells n in one direction of a cubic supercell) at 300 K. The numbers within the parentheses are statistical uncertainties for the last significant number.

n	EMD		HNEMD	
	MOF-5	MOF-5	HKUST-1	ZIF-8
2	0.30(1)	0.31(2)	0.60(3)	0.47(6)
3	0.46(2)	0.46(2)	0.78(4)	0.57(3)
4	0.54(2)	0.55(1)	0.86(2)	0.52(4)
5	0.61(2)	0.62(1)	0.89(2)	0.59(3)
6	/	0.64(1)	0.92(2)	0.59(3)

matches with the experimentally measured value of 0.64 ± 0.09 W/(m K) [14]. For HKUST-1, our predicted LTC, 0.89 ± 0.02 W/(m K) is only slightly larger than the experimentally measured value of 0.69 ± 0.05 W/(m K) [15]. For these two MOFs, the good agreement with experiments is achieved for the first time. In the case of MOF-5, we predicted a LTC of 0.62 ± 0.01 W/(m K) that is significantly higher than the experimentally measured value of 0.32 W/(m K) [7]. This discrepancy is yet to be understood and we will discuss it further below.

The finite-size effects can be understood in terms of the spectral LTC as shown in Fig. 7. With a larger simulation domain size, phonons with longer wave lengths (smaller frequencies) are brought into existence which contribute significantly in the low-frequency region. Fig. 7 shows that the contribution from phonons with $\omega/2\pi < 1$ THz is significantly reduced when the small $2 \times 2 \times 2$ supercell is used. To understand this more quantitatively, we note that the phonon group velocities for the acoustic branches are about 5 km/s, based on the spectral energy density (SED) shown in Fig. 8. Taking MOF-5 as an ex-

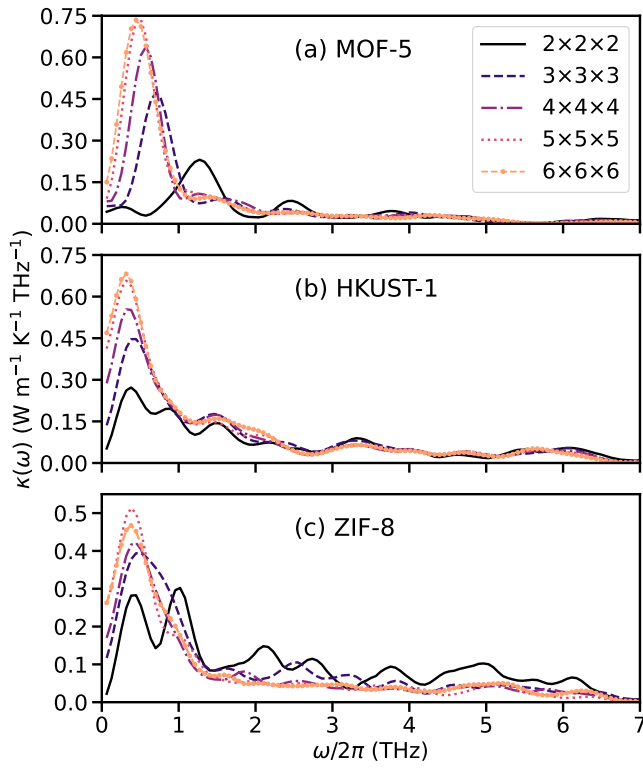


FIG. 7. Spectral LTC $\kappa(\omega)$ as a function of phonon frequency $\omega/2\pi$ for (a) MOF-5, (b) HKUST-1, and (c) ZIF-8 at 300 K calculated by using different supercell sizes.

ample, the largest phonon wave length that can exist in a $2 \times 2 \times 2$ supercell is about 5 nm and the frequency for it is about 1 THz. That is, phonons with frequencies smaller than 1 THz are largely suppressed in this supercell. With a $5 \times 5 \times 5$ supercell, phonons with $\omega/2\pi < 1$ THz can be activated and their contribution to the total LTC is almost converged. In all the three MOFs, phonons with $\omega/2\pi < 1$ THz contribute about 50% to the total LTC.

The large spectral LTCs in the low-frequency region are associated with the large phonon MFPs, as shown in Fig. 9. The maximum phonon MFPs for MOF-5, HKUST-1, and ZIF-8 are 0.17 μm , 0.28 μm , and 0.16 μm , respectively. Due to the large MFPs, the apparent LTC only saturates in the micrometre scale of system length L , as shown in the inset of Fig. 9. The slow convergence of the LTC with respect to L for HKUST-1 is further confirmed by independent NEMD simulations.

Using an empirical force field, Wieser *et al.* [33, 36] observed that the LTC of MOF-5 is not converged up to 20 nm in NEMD simulations, which is consistent to our results. This means that the large phonon MFPs in MOFs are not sensitive to the details of the interatomic potential. As we have discussed above, the large phonon MFPs in the low-frequency region means that a $2 \times 2 \times 2$ supercell is not sufficient to obtain converged LTC in EMD simulations. With this small supercell, our

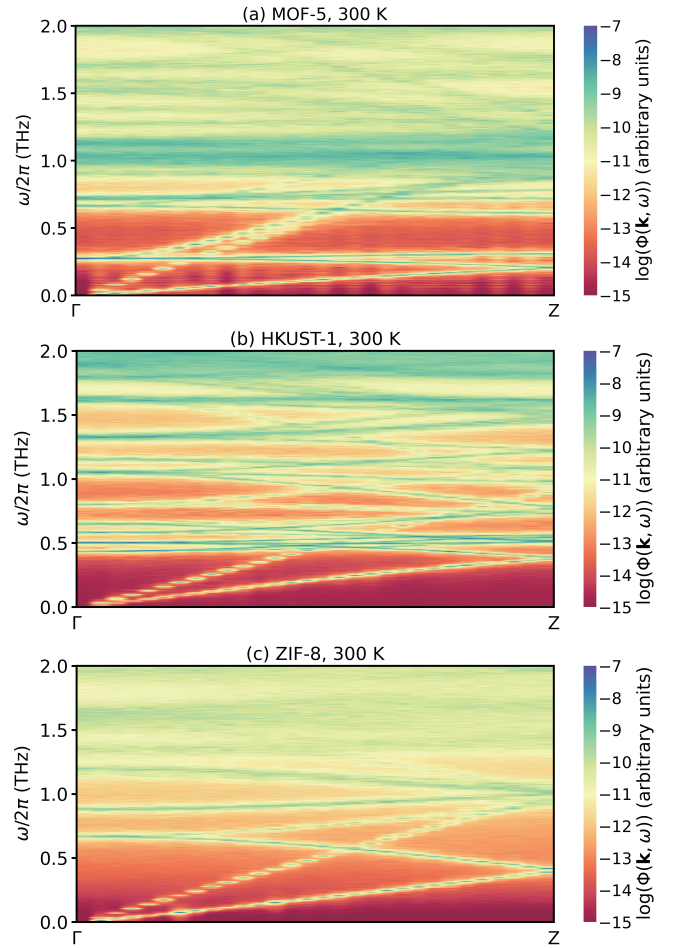


FIG. 8. Phonon SED of (a) MOF-5, (b) HKUST-1, and (c) ZIF-8 at 300 K as a function of wave number in the Γ -Z path and phonon frequency.

EMD prediction of 0.30 ± 0.01 W/(m K) is very close to the experimental value [7] of 0.32 W/(m K) as well as the previous EMD simulations [16]. However, this good agreement is most likely an accident as the LTC predicted by our EMD simulations with a $5 \times 5 \times 5$ supercell is 0.61 ± 0.02 W/(m K), which is about twice of the experimental value. A possible explanation of the discrepancy between our predictions and the previous experiment [7] is that the measured samples might not be single crystals. According to the length-scaling in the inset of Fig. 9, the LTC of MOF-5 is only about half of the converged value when L is about 0.1 μm . We therefore speculate that the experimental samples [7] might be nano-crystals with a characteristic size of 0.1 μm or contain defects that have been observed to significantly reduce the thermal conductivity of MOFs [25].

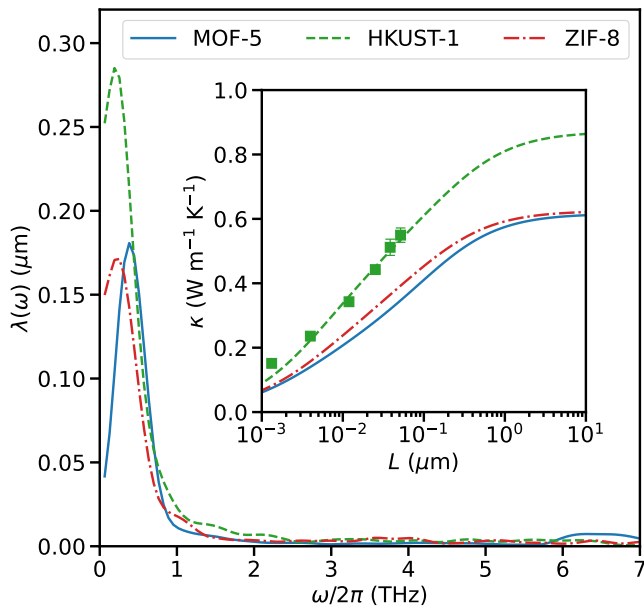


FIG. 9. Phonon MFP $\lambda(\omega)$ as a function of phonon frequency $\omega/2\pi$ for the three MOFs at 300 K. Inset: Apparent LTC $\kappa(L)$ as a function of the transport length L for the three MOFs at 300 K as calculated from the HNEMD-based spectral decomposition method (lines) and direct NEMD simulations (markers; for HKUST-1 only).

III. SUMMARY AND CONCLUSIONS

In summary, we have developed a set of accurate and highly efficient MLPs for three typical MOFs, including MOF-5, HKUST-1, and ZIF-8, using the efficient NEP approach and quantum-mechanical DFT calculations. For each MOF, the NEP model accurately reproduces the RDF and ADF as compared to DFT calculations, showing much higher accuracy than typical empirical force fields. We have performed extensive MD simulations with the NEP models to study thermal transport in these MOFs. We have mainly used the HNEMD method, but have also used the EMD and NEMD methods for crosschecking the consistency of the results.

We have carefully examined the finite-size effects in EMD and HNEMD simulations for which previous works have not paid sufficient attentions. Contrary to the common assumption that a supercell with $2 \times 2 \times 2$ conventional cells is sufficient, our results indicate that at least a $5 \times 5 \times 5$ supercell is required to achieve converged results. This is not only relevant to the calculated LTC values at a specific temperature, but also crucial for obtaining the correct temperature dependence of the LTC. Our results suggest that the LTCs of MOFs exhibit a moderate temperature dependence of $\sim T^{-0.6}$, which is not as strong as $\sim T^{-1}$ in conventional crystals, but is also not as weak as $\sim T^0$ in typical amorphous materials.

With the converged simulation cell size, we have obtained the spectral LTC within the HNEMD method and

found that phonons with frequency $\omega/2\pi < 1$ THz contribute about half to the total LTC. These phonons have sub-micrometer MFPs, which can neither be accessed by EMD simulations with a small supercell nor NEMD simulations with short domain lengths, making them largely undiscovered before.

Among the three MOFs we considered, HKUST-1 has the largest LTC, while the other two have smaller and comparable LTC. Our results for HKUST-1 and ZIF-8 are in very good agreement with experiments [14, 15], but the same has not been achieved for MOF-5 [7]. More work is needed to resolve this discrepancy.

Overall, we have obtained a clear picture of thermal transport in MOFs. They typically have a LTC smaller than $1 \text{ W}/(\text{mK})$ but there are THz-phonons with sub-micrometer MFPs that contribute a significant portion of the LTC and give rise to a strong length dependence of the apparent LTC. Therefore, the LTC in nano-crystals can be heavily reduced compared to single-crystals.

NOTES

The authors declare no competing financial interest. The source code and documentation for GPUMD are available at <https://github.com/brucefan1983/GPUMD> and <https://gpumd.org>, respectively. The source code for SED calculations is available at <https://github.com/Tingliangstu/pySED>. The training and testing results for the NEP models are freely available at <https://gitlab.com/brucefan1983/nep-data>. Representative input and output files for thermal conductivity calculations are freely available at <https://github.com/hityingph/supporting-info>.

ACKNOWLEDGMENTS

The authors would like to thank Bing Wang, Yanzhou Wang, Zezhu Zeng, and Shiyun Xiong for insightful discussions. P.Y. and Z.Z. acknowledge the National Natural Science Foundation of China (Grant No. 11932005) and the program of Innovation Team in Universities and Colleges in Guangdong (2021KCXTD006). T.L. and J.X. acknowledge the Research Grants Council of Hong Kong (Grant No. AoE/P-701/20). J.Z. acknowledges the support from the Guangdong Basic and Applied Basic Research Foundation (No.2022A1515010631). Z.F. acknowledges support from the National Natural Science Foundation of China (No. 11974059).

METHODS

1. The NEP approach

In the NEP approach, a feedforward neural network (NN) with a single hidden layer of N_{neu} neurons is used

to represent the site energy U_i of atom i as a function of a descriptor vector with N_{des} components [50]:

$$U_i = \sum_{\mu=1}^{N_{\text{neu}}} w_{\mu}^{(1)} \tanh \left(\sum_{\nu=1}^{N_{\text{des}}} w_{\mu\nu}^{(0)} q_{\nu}^i - b_{\mu}^{(0)} \right) - b^{(1)}, \quad (1)$$

where $\tanh(x)$ is the activation function, $\mathbf{w}^{(0)}$, $\mathbf{w}^{(1)}$, $\mathbf{b}^{(0)}$, and $b^{(1)}$ are the trainable weight and bias parameters in the NN. The atomic environment descriptor q_{ν}^i consists of a number of radial and angular components similar to the Behler-Parrinello approach [69]. The radial descriptor components (with a cutoff radius r_c^R) only depend on atom-pair distances and are constructed based on Chebyshev polynomials. The angular descriptor components (with a cutoff radius r_c^A) also depend on angular information and are constructed based on spherical harmonics similar to the atomic cluster expansion approach [70]. A NEP model is trained using the separable natural evolution strategy (SNES) [71] by minimizing a loss function that is defined as a weighted sum of the RMSEs of energy, force, and virial as well as terms serving as ℓ_1 and ℓ_2 regularization. For more details of the NEP approach, we refer to the literature. [50–52].

There are a number of important hyperparameters in the NEP approach that need to be carefully chosen. Based on previous publications [50–52, 72–75] and our extensive tests, we reached a set of optimized hyperparameters for the three MOFs. For all the three MOFs, we used the same hyperparameters except for the cutoff radius of the angular descriptor components r_c^A that was set to 4 Å for both MOF-5 and HKUST-1, but to 3 Å for ZIF-8. The cutoff radius of the radial descriptor components was set to a larger value of 6 Å to incorporate more neighbors. Both the radial and angular descriptor components have radial functions. For the radial descriptor components, we used 13 radial functions, each being a linear combination of 13 Chebyshev polynomials. For the angular descriptor components, we used 9 radial functions, each being a linear combination of 9 Chebyshev polynomials. For the angular descriptor components, we used both three-body and four-body correlations up to degree $l = 4$ and $l = 2$ respectively in the spherical harmonics Y_{lm} . The number of neurons in the hidden layer was chosen to be $N_{\text{neu}} = 80$, which is large enough to achieve a high accuracy.

2. Reference data generation

We employed an iterative scheme as shown in Fig. S1 to construct the training data for the NEP model of each material. While a more sophisticated method is needed for complex materials with very large primitive cells [76], it is feasible to generate the training data using the primitive cells in our case. Starting from the optimized structure of the primitive cell of a given material, we performed constant-volume DFT-driven MD simulations with the target temperature linearly increasing from 10 K

to 800 K within 10 ps (10000 steps) and sampled 560 structures. We also generated 100 structures by applying random cell deformations (-3% to 3%) and atomic displacements (within 0.1 Å) starting from the optimized structure. We performed more accurate DFT calculations (see below) for the 660 structures and obtained the initial data set and trained the first NEP model. Then we performed NEP-driven MD simulations at our intended thermodynamic conditions and selected 100 more structures based on the farthest-point sampling by comparing the distance of structures in two-dimensional (2D) principal component (PC) space. We then trained the second NEP model based on the expanded 760 structures. Another round of expansion was similarly performed and our final data set has 860 structures for each material. We have used 90% for training and 10% for testing.

The DFT-MD simulations were conducted in the isothermal (NVT) ensemble with an energy threshold of 10^{-5} eV, an energy cutoff of 520 eV for the electronic self-consistent loop, and the Γ point was sampled in the Brillouin zone. To obtain the energy, force, and virial data for NEP training, we performed DFT calculations using the Perdew-Burke-Ernzerhof functional [77] and the projector-augmented wave method [78] implemented in Vienna ab-initio simulation package package [79, 80]. We sampled the Brillouin zone with a k -point density of 0.2/Å and used Gaussian smearing with a width of 0.05 eV. For the electronic self-consistent loop, we set a threshold of 10^{-7} eV with an energy cutoff of 600 eV.

3. The HNEMD method and spectral conductivity in the diffusive regime

The HNEMD method has been shown to be one of the most efficient MD methods for obtaining diffusive thermal transport properties [54, 73, 75, 81]. In HNEMD simulation of thermal conduction in solid, an external driving force

$$\mathbf{F}_i^{\text{ext}} = \mathbf{F}_e \cdot \mathbf{W}_i. \quad (2)$$

is added to each atom i to drive the system out of equilibrium. Here \mathbf{W}_i is the virial tensor of atom i and \mathbf{F}_e is the driving force parameter which is of the dimension of inverse length. The driving force will induce a net heat current \mathbf{J} whose ensemble average (represented by $\langle \dots \rangle$ below) is proportional to the driving force parameter:

$$\frac{\langle \mathbf{J}^{\alpha} \rangle}{TV} = \sum_{\beta} \kappa^{\alpha\beta} \mathbf{F}_e^{\beta}. \quad (3)$$

where T is the system temperature, V is the system volume, and $\kappa^{\alpha\beta}$ is the $\alpha\beta$ -component of the LTC tensor. For explicit expressions of the virial tensor and heat current vector applicable to the NEP model, we refer to the literature. [45, 50, 52] In this paper, the three MOFs have cubic symmetry and without loss of generality we

can focus on the diagonal component in the x direction, giving

$$\kappa^{xx} = \frac{\langle J^x \rangle}{TVF_e^x}. \quad (4)$$

The magnitude of the driving force parameter F_e needs to be small enough to keep the system within the linear-response regime but also large enough to induce a sufficiently large signal-to-noise ratio. We have tested that for all the three MOFs $F_e^x = 2 \times 10^{-4}/\text{\AA}$ is an appropriate value for temperatures ≥ 300 K, while a slightly smaller value of $F_e^x = 1.5 \times 10^{-4}/\text{\AA}$ is more appropriate for lower temperatures.

An appealing feature of the HNEMD method is that the LTC can be spectrally decomposed [54]:

$$\kappa^{xx} = \int_0^\infty \frac{d\omega}{2\pi} \kappa^{xx}(\omega), \quad (5)$$

where

$$\kappa^{xx}(\omega) = \frac{2}{VTF_e^x} \int_{-\infty}^\infty dt e^{i\omega t} K^x(t). \quad (6)$$

Here, $K^x(t)$ is the x -component of the virial-velocity correlation function:

$$\mathbf{K}(t) = \sum_i \langle \mathbf{W}_i(0) \cdot \mathbf{v}_i(t) \rangle. \quad (7)$$

where \mathbf{v}_i is the velocity of atom i .

4. The NEMD method and spectral conductance in the ballistic regime

With the HNEMD method alone, one can only access the diffusive transport properties. To obtain a more complete description of thermal transport from ballistic to diffusive, an established efficient scheme [54, 82] is to supplement HNEMD with NEMD simulations.

In our NEMD simulations, two local thermostats, i.e., heat source and heat sink, at different temperatures are used to generate a non-equilibrium steady state with constant heat flux. The thermal conductance G between the two thermostats separated by distance L can be calculated as:

$$G^{xx}(L) = \frac{J^x}{\Delta TV}, \quad (8)$$

where ΔT is the temperature difference between the heat source and the heat sink. An effective LTC (also called apparent LTC) $\kappa^{xx}(L)$ for the finite system with a transport length of L can be defined as [82]:

$$\kappa^{xx}(L) = G^{xx}(L)L = \frac{J^x}{(\Delta T/L)V}. \quad (9)$$

Similar to the LTC, the thermal conductance can also be spectrally decomposed:

$$G^{xx}(L) = \int_0^\infty \frac{d\omega}{2\pi} G^{xx}(L, \omega), \quad (10)$$

where

$$G^{xx}(L, \omega) = \frac{2}{V\Delta T} \int_{-\infty}^\infty dt e^{i\omega t} K^x(t). \quad (11)$$

The limit of zero transport length $L \rightarrow 0$ corresponds to the ballistic limit $G_b^{xx}(\omega) = G^{xx}(L \rightarrow 0, \omega)$, and one can define a spectrally decomposed MFP as $\lambda^{xx}(\omega) = \kappa^{xx}(\omega)/G_b^{xx}(\omega)$. With the spectral MFP, we can obtain the spectral LTC with any transport length

$$\kappa^{xx}(L, \omega) = \frac{\kappa^{xx}(\omega)}{1 + \lambda^{xx}(\omega)/L}, \quad (12)$$

and the integrated LTC

$$\kappa^{xx}(L) = \int_0^\infty \frac{d\omega}{2\pi} \kappa^{xx}(L, \omega). \quad (13)$$

5. The EMD method

In the EMD method based on a Green-Kubo relation, [41, 42] the xx -component of the running LTC can be expressed as an integral of the heat current auto-correlation function:

$$\kappa^{xx}(t) = \frac{1}{k_B T^2 V} \int_0^t dt' \langle J^x(0) J^x(t') \rangle, \quad (14)$$

where k_B is Boltzmann's constant and t is the upper limit of the correlation time.

6. Phonon SED calculations

We perform the phonon SED [83, 84] calculations to examine the phonon dispersion structures of MOFs. The phonon SED is a function of wave vector (\mathbf{k}) and frequency (ω), and can be calculated using the following formula in MD simulations:

$$\begin{aligned} \Phi(\mathbf{k}, \omega) &= \frac{1}{4\pi\tau_0 N} \sum_{\alpha}^{\{x,y,z\}} \sum_b^B m_b \\ &\times \left| \int_0^{\tau_0} \sum_{n_{x,y,z}}^N v_{\alpha} \left(\begin{matrix} n_{x,y,z} \\ b \end{matrix}; t \right) \right. \\ &\times \exp \left[i\mathbf{k} \cdot \mathbf{r} \left(\begin{matrix} n_{x,y,z} \\ 0 \end{matrix} \right) - i\omega t \right] dt \Big|^2, \end{aligned} \quad (15)$$

where τ_0 is the total simulation time, N is the number of unit cells in the crystal, b is the atom label in a given unit

cell n , m_b is the mass of atom b in the unit cell, $n_{x,y,z}$ is the index number of unit cells along the x , y , and z directions, $v_\alpha \left(\begin{smallmatrix} n_{x,y,z} \\ b \end{smallmatrix}; t \right)$ denotes the velocity of atom b of the n -th unit cell along the α direction at time t and $\mathbf{r} \left(\begin{smallmatrix} n_{x,y,z} \\ 0 \end{smallmatrix} \right)$ is the equilibrium position of unit cell n .

7. Details of the MD simulations

We used the GPUMD package (version 3.7) [53] to perform all the MD simulations. A time step of 0.5 fs was used with the velocity-Verlet integration scheme, which has been confirmed to be small enough. The time coupling parameter in the thermostat and barostat are 50 fs and 500 fs, respectively. In all HNEMD, EMD, and NEMD simulations, we calculated the statistical error of the LTC as the standard error of the mean values from five independent runs.

a. HNEMD simulations

In HNEMD simulations, we first equilibrated for 100 ps in the isothermal-isobaric (NpT) ensemble at a given target temperature and zero pressure, followed by a 2 ns production stage in the NVT ensemble. The NpT ensemble was achieved by the Berendsen method [85]. The NVT ensemble was achieved by the Nose-Hoover chain thermostat [86]. The external driving force was added during the production stage.

b. NEMD simulations

In NEMD simulations, the system was only periodic in the lateral directions and the two ends in the transport direction were fixed. Next to one fixed end, a heat source region with a temperature of 325 K was created by applying a Langevin thermostat [87] and a heat sink region with a temperature of 275 K was similarly created next to the other fixed end. The thermostated regions contain two conventional cells in the transport direction which are sufficiently long to avoid artifacts [82]. After an equilibration similar to the HNEMD simulation, the NEMD simulation with the two local Langevin thermostats was performed for 1 ns. All the simulated samples have 5×5 conventional cells in the lateral directions and the lengths in the transport direction are varied to explore different transport regimes.

c. EMD simulations

In EMD simulations, after an equilibration similar to the HNEMD simulation, a production run in the microcanonical (NVE) ensemble was performed for 10 ns.

d. Phonon SED calculations

For the phonon SED calculations, we used a $1 \times 1 \times 60$ supercell for each MOF. All systems were first relaxed in the NVT ensemble for 0.5 ns, followed by a 0.75 ns production stage in the NVE ensemble. The velocities and positions of all atoms during the final 0.5 ns were collected to calculate the SED.

-
- [1] J. L. Rowsell and O. M. Yaghi, Metal-organic frameworks: a new class of porous materials, *Microporous and Mesoporous Materials* **73**, 3 (2004).
- [2] O. M. Yaghi, M. O’Keeffe, N. W. Ockwig, H. K. Chae, M. Eddaoudi, and J. Kim, Reticular synthesis and the design of new materials, *Nature* **423**, 705 (2003).
- [3] B. Li, H.-M. Wen, W. Zhou, and B. Chen, Porous metal-organic frameworks for gas storage and separation: what, how, and why?, *The Journal of Physical Chemistry Letters* **5**, 3468 (2014).
- [4] N. Hanikel, M. S. Prévot, and O. M. Yaghi, MOF water harvesters, *Nature Nanotechnology* **15**, 348 (2020).
- [5] I. Stassen, N. Burtch, A. Talin, P. Falcaro, M. Allendorf, and R. Ameloot, An updated roadmap for the integration of metal-organic frameworks with electronic devices and chemical sensors, *Chemical Society Reviews* **46**, 3185 (2017).
- [6] S. M. Rogge, A. Bavykina, J. Hajek, H. Garcia, A. I. Olivos-Suarez, A. Sepúlveda-Escribano, A. Vimont, G. Clet, P. Bazin, F. Kapteijn, *et al.*, Metal-organic and covalent organic frameworks as single-site catalysts, *Chemical Society Reviews* **46**, 3134 (2017).
- [7] B. Huang, Z. Ni, A. Millward, A. McGaughey, C. Uher, M. Kaviani, and O. Yaghi, Thermal conductivity of a metal-organic framework (MOF-5): Part II. Measurement, *International Journal of Heat and Mass Transfer* **50**, 405 (2007).
- [8] Y. Ming, J. Purewal, A. Sudik, C. Xu, J. Yang, M. Veenstra, K. Rhodes, R. Soltis, J. Warner, M. Gaab, *et al.*, Thermophysical properties of MOF-5 powders, *Microporous and Mesoporous Materials* **185**, 235 (2014).
- [9] K. J. Erickson, F. Léonard, V. Stavila, M. E. Foster, C. D. Spataru, R. E. Jones, B. M. Foley, P. E. Hopkins, M. D. Allendorf, and A. A. Talin, Thin film thermoelectric metal-organic framework with high seebeck coefficient and low thermal conductivity, *Advanced Materials* **27**, 3453 (2015).
- [10] T. A. Semelsberger, M. Veenstra, and C. Dixon, Room temperature thermal conductivity measurements of neat MOF-5 compacts with high pressure hydrogen and helium, *International Journal of Hydrogen Energy* **41**, 4690 (2016).
- [11] W. D. Gunatilleke, K. Wei, Z. Niu, L. Wojtas, G. Nolas, and S. Ma, Thermal conductivity of a perovskite-type metal-organic framework crystal, *Dalton Transactions* **46**, 13342 (2017).
- [12] L. Sun, B. Liao, D. Sheberla, D. Kraemer, J. Zhou, E. A. Stach, D. Zakharov, V. Stavila, A. A. Talin, Y. Ge, *et al.*,

- A microporous and naturally nanostructured thermoelectric metal-organic framework with ultralow thermal conductivity, *Joule* **1**, 168 (2017).
- [13] J. Huang, X. Xia, X. Hu, S. Li, and K. Liu, A general method for measuring the thermal conductivity of mof crystals, *International Journal of Heat and Mass Transfer* **138**, 11 (2019).
- [14] J. Huang, A. Fan, X. Xia, S. Li, and X. Zhang, In situ thermal conductivity measurement of single-crystal zeolitic imidazolate framework-8 by raman-resistance temperature detectors method, *ACS Nano* **14**, 14100 (2020).
- [15] H. Babaei, M. E. DeCoster, M. Jeong, Z. M. Hassan, T. Islamoglu, H. Baumgart, A. J. McGaughey, E. Redel, O. K. Farha, P. E. Hopkins, *et al.*, Observation of reduced thermal conductivity in a metal-organic framework due to the presence of adsorbates, *Nature Communications* **11**, 1 (2020).
- [16] B. Huang, A. McGaughey, and M. Kaviani, Thermal conductivity of metal-organic framework 5 (MOF-5): Part I. Molecular dynamics simulations, *International Journal of Heat and Mass Transfer* **50**, 393 (2007).
- [17] X. Zhang and J. Jiang, Thermal conductivity of zeolitic imidazolate framework-8: A molecular simulation study, *The Journal of Physical Chemistry C* **117**, 18441 (2013).
- [18] L. Han, M. Budge, and P. A. Greaney, Relationship between thermal conductivity and framework architecture in MOF-5, *Computational Materials Science* **94**, 292 (2014).
- [19] H. Babaei and C. E. Wilmer, Mechanisms of heat transfer in porous crystals containing adsorbed gases: Applications to metal-organic frameworks, *Physical Review Letters* **116**, 025902 (2016).
- [20] H. Babaei, A. J. McGaughey, and C. E. Wilmer, Effect of pore size and shape on the thermal conductivity of metal-organic frameworks, *Chemical Science* **8**, 583 (2017).
- [21] K. B. Sezginel, P. A. Asinger, H. Babaei, and C. E. Wilmer, Thermal transport in interpenetrated metal-organic frameworks, *Chemistry of Materials* **30**, 2281 (2018).
- [22] J. Wieme, S. Vandenbrande, A. Lemaire, V. Kapil, L. Vanduyffhuys, and V. Van Speybroeck, Thermal engineering of metal-organic frameworks for adsorption applications: a molecular simulation perspective, *ACS Applied Materials & Interfaces* **11**, 38697 (2019).
- [23] W. Wei, J. Huang, W. Li, H. Peng, and S. Li, Impacts of ethanol and water adsorptions on thermal conductivity of ZIF-8, *The Journal of Physical Chemistry C* **123**, 27369 (2019).
- [24] S. S. Sørensen, M. B. Østergaard, M. Stepniewska, H. Johra, Y. Yue, and M. M. Smedskjaer, Metal-organic framework glasses possess higher thermal conductivity than their crystalline counterparts, *ACS Applied Materials & Interfaces* **12**, 18893 (2020).
- [25] M. Islamov, H. Babaei, and C. E. Wilmer, Influence of missing linker defects on the thermal conductivity of metal-organic framework HKUST-1, *ACS Applied Materials & Interfaces* **12**, 56172 (2020).
- [26] K. B. Sezginel, S. Lee, H. Babaei, and C. E. Wilmer, Effect of flexibility on thermal transport in breathing porous crystals, *The Journal of Physical Chemistry C* **124**, 18604 (2020).
- [27] H. Babaei, J.-H. Lee, M. N. Dods, C. E. Wilmer, and J. R. Long, Enhanced thermal conductivity in a diamine-appended metal-organic framework as a result of cooperative CO₂ adsorption, *ACS Applied materials & Interfaces* **12**, 44617 (2020).
- [28] P. Ying, J. Zhang, X. Zhang, and Z. Zhong, Impacts of functional group substitution and pressure on the thermal conductivity of ZIF-8, *The Journal of Physical Chemistry C* **124**, 6274 (2020).
- [29] P. Ying, J. Zhang, and Z. Zhong, Effect of phase transition on the thermal transport in isorecticular dut materials, *The Journal of Physical Chemistry C* **125**, 12991 (2021).
- [30] R. Cheng, W. Li, W. Wei, J. Huang, and S. Li, Molecular insights into the correlation between microstructure and thermal conductivity of zeolitic imidazolate frameworks, *ACS Applied Materials & Interfaces* **13**, 14141 (2021).
- [31] S. Zhang, J. Liu, and L. Liu, Insights into the thermal conductivity of MOF-5 from first principles, *RSC Advances* **11**, 36928 (2021).
- [32] A. Lemaire, J. Wieme, A. E. Hoffman, and V. Van Speybroeck, Atomistic insight in the flexibility and heat transport properties of the stimuli-responsive metal-organic framework MIL-53 (Al) for water-adsorption applications using molecular simulations, *Faraday Discussions* **225**, 301 (2021).
- [33] S. Wieser, T. Kamencek, J. P. Dürholt, R. Schmid, N. Bedoya-Martínez, and E. Zojer, Identifying the bottleneck for heat transport in metal-organic frameworks, *Advanced Theory and Simulations* **4**, 2000211 (2021).
- [34] Y. Zhou, B. Huang, and B.-Y. Cao, Vibrational modes with long mean free path and large volumetric heat capacity drive higher thermal conductivity in amorphous zeolitic imidazolate framework-4, *Materials Today Physics* **21**, 100516 (2021).
- [35] Y. Zhou, Y. Xu, Y. Gao, and S. Volz, Origin of the weakly temperature-dependent thermal conductivity in ZIF-4 and ZIF-62, *Physical Review Materials* **6**, 015403 (2022).
- [36] S. Wieser, T. Kamencek, R. Schmid, N. Bedoya-Martínez, and E. Zojer, Exploring the Impact of the Linker Length on Heat Transport in Metal-Organic Frameworks, *Nanomaterials* **12**, 2142 (2022).
- [37] H. Fan, C. Yang, and Y. Zhou, Ultralong mean free path phonons in HKUST-1 and their scattering by water adsorbates, *Physical Review B* **106**, 085417 (2022).
- [38] H. Li, M. Eddaoudi, M. O’Keeffe, and O. M. Yaghi, Design and synthesis of an exceptionally stable and highly porous metal-organic framework, *Nature* **402**, 276 (1999).
- [39] X.-C. Huang, Y.-Y. Lin, J.-P. Zhang, and X.-M. Chen, Ligand-directed strategy for zeolite-type metal-organic frameworks: zinc (II) imidazolates with unusual zeolitic topologies, *Angewandte Chemie International Edition* **45**, 1557 (2006).
- [40] S. S.-Y. Chui, S. M.-F. Lo, J. P. Charmant, A. G. Orpen, and I. D. Williams, A chemically functionalizable nanoporous material [Cu₃ (TMA)₂ (H₂O)₃]_n, *Science* **283**, 1148 (1999).
- [41] M. S. Green, Markoff random processes and the statistical mechanics of time-dependent phenomena. ii. irreversible processes in fluids, *The Journal of Chemical Physics* **22**, 398 (1954).
- [42] R. Kubo, Statistical-mechanical theory of irreversible processes. i. general theory and simple applications to magnetic and conduction problems, *Journal of the Physical Society of Japan* **12**, 570 (1957).

- [43] A. Stukowski, Visualization and analysis of atomistic simulation data with OVITO—the Open Visualization Tool, *Modelling and Simulation in Materials Science and Engineering* **18**, 015012 (2009).
- [44] A. P. Thompson, H. M. Aktulga, R. Berger, D. S. Bolintineanu, W. M. Brown, P. S. Crozier, P. J. in't Veld, A. Kohlmeyer, S. G. Moore, T. D. Nguyen, *et al.*, LAMMPS—a flexible simulation tool for particle-based materials modeling at the atomic, meso, and continuum scales, *Computer Physics Communications* **271**, 108171 (2022).
- [45] Z. Fan, L. F. C. Pereira, H.-Q. Wang, J.-C. Zheng, D. Donadio, and A. Harju, Force and heat current formulas for many-body potentials in molecular dynamics simulations with applications to thermal conductivity calculations, *Physical Review B* **92**, 094301 (2015).
- [46] O. Tayfuroglu, A. Kocak, and Y. Zorlu, A neural network potential for the IRMOF series and its application for thermal and mechanical behaviors, *Physical Chemistry Chemical Physics* **24**, 11882 (2022).
- [47] S. Vandenhoute, M. Cools-Ceuppens, S. DeKeyser, T. Verstraelen, and V. Van Speybroeck, Machine learning potentials for metal-organic frameworks using an incremental learning approach, *npj Computational Materials* **9**, 19 (2023).
- [48] S. K. Achar, J. J. Wardzala, L. Bernasconi, L. Zhang, and J. K. Johnson, Combined deep learning and classical potential approach for modeling diffusion in UiO-66, *Journal of Chemical Theory and Computation* **18**, 3593 (2022).
- [49] B. Zheng, F. L. Oliveira, R. Neumann Barros Ferreira, M. Steiner, H. Hamann, G. X. Gu, and B. Luan, Quantum Informed Machine-Learning Potentials for Molecular Dynamics Simulations of CO₂'s Chemisorption and Diffusion in Mg-MOF-74, *ACS Nano* **10.1021/acsnano.2c11102** (2023).
- [50] Z. Fan, Z. Zeng, C. Zhang, Y. Wang, K. Song, H. Dong, Y. Chen, and T. Ala-Nissila, Neuroevolution machine learning potentials: Combining high accuracy and low cost in atomistic simulations and application to heat transport, *Physical Review B* **104**, 104309 (2021).
- [51] Z. Fan, Improving the accuracy of the neuroevolution machine learning potential for multi-component systems, *Journal of Physics: Condensed Matter* **34**, 125902 (2022).
- [52] Z. Fan, Y. Wang, P. Ying, K. Song, J. Wang, Y. Wang, Z. Zeng, K. Xu, E. Lindgren, J. M. Rahm, A. J. Gabourie, J. Liu, H. Dong, J. Wu, Y. Chen, Z. Zhong, J. Sun, P. Erhart, Y. Su, and T. Ala-Nissila, GPUMD: A package for constructing accurate machine-learned potentials and performing highly efficient atomistic simulations, *The Journal of Chemical Physics* **157**, 114801 (2022).
- [53] Z. Fan, W. Chen, V. Vierimaa, and A. Harju, Efficient molecular dynamics simulations with many-body potentials on graphics processing units, *Computer Physics Communications* **218**, 10 (2017).
- [54] Z. Fan, H. Dong, A. Harju, and T. Ala-Nissila, Homogeneous nonequilibrium molecular dynamics method for heat transport and spectral decomposition with many-body potentials, *Physical Review B* **99**, 064308 (2019).
- [55] M. A. Addicoat, N. Vankova, I. F. Akter, and T. Heine, Extension of the universal force field to metal-organic frameworks, *Journal of Chemical Theory and Computation* **10**, 880 (2014).
- [56] P. G. Boyd, S. M. Moosavi, M. Witman, and B. Smit, Force-field prediction of materials properties in metal-organic frameworks, *The journal of physical chemistry letters* **8**, 357 (2017).
- [57] R. Pallach, J. Keupp, K. Terlinden, L. Frenzel-Beyme, M. Kloß, A. Machalica, J. Kotschy, S. K. Vasa, P. A. Chater, C. Sternemann, *et al.*, Frustrated flexibility in metal-organic frameworks, *Nature communications* **12**, 4097 (2021).
- [58] S. Bureekaew, S. Amirjalayer, M. Tafipolsky, C. Spickermann, T. K. Roy, and R. Schmid, MOF-FF—A flexible first-principles derived force field for metal-organic frameworks, *physica status solidi (b)* **250**, 1128 (2013).
- [59] J. P. Dürholt, G. Fraux, F.-X. Coudert, and R. Schmid, Ab initio derived force fields for zeolitic imidazolate frameworks: MOF-FF for ZIFs, *Journal of Chemical Theory and Computation* **15**, 2420 (2019).
- [60] S. Monti, C. Li, and V. Carravetta, Reactive dynamics simulation of monolayer and multilayer adsorption of glycine on Cu (110), *The Journal of Physical Chemistry C* **117**, 5221 (2013).
- [61] S. S. Han, S.-H. Choi, and A. C. Van Duin, Molecular dynamics simulations of stability of metal-organic frameworks against H₂O using the ReaxFF reactive force field, *Chemical communications* **46**, 5713 (2010).
- [62] Y. Yang, Y. K. Shin, S. Li, T. D. Bennett, A. C. Van Duin, and J. C. Mauro, Enabling computational design of ZIFs using ReaxFF, *The Journal of Physical Chemistry B* **122**, 9616 (2018).
- [63] A. C. Van Duin, S. Dasgupta, F. Lorant, and W. A. Goddard, ReaxFF: a reactive force field for hydrocarbons, *The Journal of Physical Chemistry A* **105**, 9396 (2001).
- [64] K. Banlusan, E. Antillon, and A. Strachan, Mechanisms of Plastic Deformation of Metal-Organic Framework-5, *The Journal of Physical Chemistry C* **119**, 25845 (2015).
- [65] M. Islamov, H. Babaei, R. Anderson, K. B. Sezginel, J. R. Long, A. J. McGaughey, D. A. Gomez-Gualdrón, and C. E. Wilmer, High-throughput screening of hypothetical metal-organic frameworks for thermal conductivity, *npj Computational Materials* **9**, 11 (2023).
- [66] J. D. Evans, J. P. Dürholt, S. Kaskel, and R. Schmid, Assessing negative thermal expansion in mesoporous metal-organic frameworks by molecular simulation, *Journal of Materials Chemistry A* **7**, 24019 (2019).
- [67] B. Wang, P. Ying, and J. Zhang, Effects of Missing Linker Defects on the Elastic Properties and Mechanical Stability of the Metal-Organic Framework HKUST-1, *The Journal of Physical Chemistry C* **127**, 2533 (2023).
- [68] N. Castel and F.-X. Coudert, Atomistic Models of Amorphous Metal-Organic Frameworks, *The Journal of Physical Chemistry C* **126**, 6905 (2022).
- [69] J. Behler and M. Parrinello, Generalized neural-network representation of high-dimensional potential-energy surfaces, *Physical Review Letters* **98**, 146401 (2007).
- [70] R. Drautz, Atomic cluster expansion for accurate and transferable interatomic potentials, *Physical Review B* **99**, 014104 (2019).
- [71] T. Schaul, T. Glasmachers, and J. Schmidhuber, High Dimensions and Heavy Tails for Natural Evolution Strategies, in *Proceedings of the 13th Annual Conference on Genetic and Evolutionary Computation*, GECCO '11 (Association for Computing Machinery, New York, NY, USA, 2011) pp. 845–852.

- [72] Y. Wang, Z. Fan, P. Qian, M. A. Caro, and T. Ala-Nissila, Quantum-corrected thickness-dependent thermal conductivity in amorphous silicon predicted by machine learning molecular dynamics simulations, *Physical Review B* **107**, 054303 (2023).
- [73] P. Ying, T. Liang, K. Xu, J. Xu, Z. Fan, T. Ala-Nissila, and Z. Zhong, Variable thermal transport in black, blue, and violet phosphorene from extensive atomistic simulations with a neuroevolution potential, *International Journal of Heat and Mass Transfer* **202**, 123681 (2023).
- [74] P. Ying, H. Dong, T. Liang, Z. Fan, Z. Zhong, and J. Zhang, Atomistic insights into the mechanical anisotropy and fragility of monolayer fullerene networks using quantum mechanical calculations and machine-learning molecular dynamics simulations, *Extreme Mechanics Letters* **58**, 101929 (2023).
- [75] H. Dong, C. Cao, P. Ying, Z. Fan, P. Qian, and Y. Su, Anisotropic and high thermal conductivity in monolayer quasi-hexagonal fullerene: A comparative study against bulk phase fullerene, *International Journal of Heat and Mass Transfer* **206**, 123943 (2023).
- [76] M. Eckhoff and J. Behler, From molecular fragments to the bulk: development of a neural network potential for MOF-5, *Journal of Chemical Theory and Computation* **15**, 3793 (2019).
- [77] J. P. Perdew, K. Burke, and M. Ernzerhof, Generalized gradient approximation made simple, *Physical Review Letters* **77**, 3865 (1996).
- [78] P. E. Blöchl, Projector augmented-wave method, *Physical Review B* **50**, 17953 (1994).
- [79] G. Kresse and J. Furthmüller, Efficient iterative schemes for ab initio total-energy calculations using a plane-wave basis set, *Physical Review B* **54**, 11169 (1996).
- [80] G. Kresse and D. Joubert, From ultrasoft pseudopotentials to the projector augmented-wave method, *Physical Review B* **59**, 1758 (1999).
- [81] P. Ying, T. Liang, Y. Du, J. Zhang, X. Zeng, and Z. Zhong, Thermal transport in planar sp²-hybridized carbon allotropes: A comparative study of biphenylene network, pentaheptite and graphene, *International Journal of Heat and Mass Transfer* **183**, 122060 (2022).
- [82] Z. Li, S. Xiong, C. Sievers, Y. Hu, Z. Fan, N. Wei, H. Bao, S. Chen, D. Donadio, and T. Ala-Nissila, Influence of thermostatting on nonequilibrium molecular dynamics simulations of heat conduction in solids, *The Journal of Chemical Physics* **151**, 234105 (2019).
- [83] J. A. Thomas, J. E. Turney, R. M. Iutzi, C. H. Amon, and A. J. H. McGaughey, Predicting phonon dispersion relations and lifetimes from the spectral energy density, *Physical Review B* **81**, 081411 (2010).
- [84] T. Feng, B. Qiu, and X. Ruan, Anharmonicity and necessity of phonon eigenvectors in the phonon normal mode analysis, *Journal of Applied Physics* **117**, 195102 (2015).
- [85] H. J. Berendsen, J. v. Postma, W. F. Van Gunsteren, A. DiNola, and J. R. Haak, Molecular dynamics with coupling to an external bath, *The Journal of Chemical Physics* **81**, 3684 (1984).
- [86] M. Tuckerman, *Statistical mechanics: theory and molecular simulation* (Oxford university press, 2010).
- [87] G. Bussi and M. Parrinello, Accurate sampling using Langevin dynamics, *Physical Review E* **75**, 056707 (2007).